IMPACT OF MODELING ASSUMPTIONS ON SIMULATED MELT POOL DYNAMICS COMPARED TO HIGH-SPEED X-RAY OBSERVATIONS

J. PLEWINSKI*[1], F. HENNIG**[2], C. FORSTER***[3], S. BELOUSOV****[4], A. ZAKIROV****[5], B. KORNEEV****[6], C. SPURK*****[7], M. HUMMEL*****,******[8], A. OLOWINSKY******[9], F. BECKMANN*******[10], J. MOOSMANN*******[11], M. SCHMIDT***[12], H. KÖSTLER**[13], M. MARKL*[14]

*Chair of Materials Science and Engineering for Metals, Friedrich-Alexander-Universität Erlangen-Nürnberg, 91058 Erlangen, Germany, ([1] 0000-0002-4815-7643, jonas.plewinski@fau.de; [14] 0000-0002-3000-7081)
**Chair for System Simulation, Friedrich-Alexander-Universität Erlangen-Nürnberg, 91058 Erlangen, Germany, ([2] 0000-0001-5298-7968; [13] 0000-0002-6992-2690)
***Institute of Photonic Technologies, Friedrich-Alexander-Universität Erlangen-Nürnberg, 91052 Erlangen, Germany, ([3] 0009-0005-9928-8001; [12] 0000-0002-8072-8768)
****Hipercone Ltd., 9434314 Jerusalem, Israel, ([4] 0000-0002-1730-5738; [5] 0000-0001-7346-6635; [6] 0000-0003-1010-6629)
*****Chair for Laser Technology, RWTH Aachen University, 52074 Aachen, Germany ([7] 0000-0002-5190-4187; [8] 0000-0002-9097-9843)
******Fraunhofer Institute for Laser Technology, 52074 Aachen, Germany ([8] 0000-0002-9097-9843; [9] 0000-0002-5231-8251)
*******Institute of Materials Physics, Helmholtz-Zentrum Hereon, 21502 Geesthacht, Germany ([10] 0000-0002-2266-9173; [11] 0000-0002-6761-7182)

DOI 10.3217/978-3-99161-089-2-009, license CC BY 4.0

ABSTRACT

Laser beam welding is a widely used advanced manufacturing process for joining metallic components across various industries. The process is prone to various defects, with solidification cracks being among the most common. Understanding the evolution of the solidification front, including temperature gradients, cooling rates and solidification velocity, is crucial to assess the conditions leading to crack formation. Direct experimental measurement of transient solidification conditions is extremely challenging, while numerical simulations of melt pool dynamics provide complementary insights by predicting local solidification conditions.

In this work, we combine high-speed synchrotron X-ray imaging, which captures the evolution and velocity of the solidification front, with state-of-the-art numerical melt pool simulations that are able to provide local solidification conditions. Comparison of experiments and simulations reveals a mismatch in the quasi-stationary welding regime, primarily arising from the neglect of the gas phase in the simulations. Using a reduced model and simulation setup, we demonstrate how changes in modeling assumptions influence melt pool dynamics and shape. Our results highlight that, for deep-penetration laser welding, proper physical modeling of the vapor-filled keyhole is essential for accurate predictions of melt pool and solidification conditions.

Keywords: Laser Beam Welding, Keyhole, Steel, Numerical Simulation, Lattice Boltzmann Method, High Performance Computing, GPU

INTRODUCTION

Laser beam welding (LBW) is a widely used advanced manufacturing process for joining metallic components across various industries, including automotive, aerospace, and medical devices. Its advantages include high power density, precise heat input control, high welding speed, and minimal heat-affected zones, enabling the joining of challenging materials and complex geometries [1].

Despite its benefits, LBW is susceptible to various defects, with solidification cracks being one common welding error. Solidification cracks are a type of hot crack that forms in the mushy zone during the final stages of solidification, where thermal stresses and strains interact with the fragile, partially solidified microstructure. These cracks evolve when the residual melt in the solidifying material cannot accommodate the tensile stresses induced by thermal contraction and solidification shrinkage. A detailed understanding of the solidification front, including the temperature gradient and solidification velocity, is crucial as these parameters dictate the local solidification conditions and the resulting microstructure, which in turn influence crack susceptibility [2-6].

The solidification conditions are mainly driven by the melt pool dynamics, as they control the heat distribution and mass transport [7]. The keyhole, a vapor-filled cavity formed by the intense laser energy, acts as a primary heat source and its stability and shape significantly influence the melt pool flow and temperature distribution. Changes in keyhole behavior, such as oscillations or collapse, can lead to melt pool instabilities, affecting the solidification front and potentially causing defects like porosity and cracking [8-11].

Experimentally measuring the transient solidification conditions and keyhole dynamics during LBW is extremely challenging due to high temperatures, small spatial scales, and rapid process rates. However, advanced investigations techniques based on synchrotron radiation have provided invaluable insights into these phenomena. Work conducted at facilities like DESY (Deutsches Elektronen-Synchrotron) has utilized high-speed X-ray imaging to track the keyhole shape and melt pool dynamics in situ during LBW. This data allows for the interpretation of process behavior, providing quantitative information on keyhole geometry, melt pool flow patterns, and even estimations of solidification velocities [12-15].

Given the experimental difficulties, numerical simulations of melt pool dynamics offer a suitable and powerful approach to investigate the solidification conditions during LBW in more detail. These simulations can provide crucial information about the solidification

velocity and temperature gradients at the solidification front, which are essential for predicting the resulting microstructure and crack probability. Various numerical approaches have been developed for LBW simulation. Latest models take different combinations of the following phenomena into account: phase changes (evaporation and condensation), compressible gas phase dynamics, beam propagation by means of ray tracing (multiple reflections of the laser beam within the keyhole) and thermo-dynamic properties of the metal vapor [16-24]. However, the optical interaction between the laser beam and the metal vapor itself, particularly absorption and attenuation mechanisms within the metal vapor, is only rarely incorporated in a physically consistent manner [25]. In most existing models, this effect is neglected, although it can significantly influence the redistribution of laser energy inside the keyhole and thereby affect both penetration depth and keyhole geometry [25, 26].

In this work, we combine high-speed synchrotron X-ray imaging with numerical melt pool simulations to investigate melt pool dynamics during LBW under quasi-stationary deep-penetration conditions. In addition to a state-of-the-art simulation approach, we introduce a reduced framework that allows systematic variation of boundary conditions along a predefined vapor capillary. The remainder of this manuscript is structured as follows. First, the experimental setup and synchrotron X-ray measurements are described. Subsequently, the numerical modeling approaches, including both the state-of-the-art simulation and the simplified framework, are introduced. Finally, experimental and numerical results are presented and discussed with respect to melt pool dynamics.

METHODS

MATERIAL

All experiments and simulations of this work are conducted with stainless steel 1.4301. The necessary material parameters for the simulations are obtained from the JMatPro[1] software. The calculation was performed through the "Stainless Steel" module, incorporating a measured chemical composition of the material in Table 1. Solidification behavior was specifically analyzed via the "Solidification Module". The simulation was initialized with a starting temperature of 3000 K and concluded at an end temperature of 298 K, employing a temperature step size of 5 K. A fraction of liquid cut-off of 0.01 was applied, and all relevant phases were considered in the calculation. A cooling rate of 10,000 K s^{-1} was specified, and an austenite grain size of 500 μm was assumed for the simulation.

[1] www.sentesoftware.co.uk/

Table 1 Chemical composition of 1.4301 in wt-%.

C	Si	Mn	P	S	Cr	N	Ni	Fe
0.02	0.41	1.6	0.028	<0.002	19.09	0.095	8.06	balance

The constant material parameters are listed in Table 2. The thermal diffusivity is computed by $\alpha = \lambda/(\rho \cdot c_p)$. The liquid phase fraction is shown in Fig. 1. The liquidus temperature is 1735 K and the solidus temperature is defined at 15 % residual liquid at 1690 K. For all simulations, the liquid phase fraction - as well as respectively the solid phase fraction - is linearly interpolated. The temperature dependent surface tension (see Fig. 1) is approximated by a linear regression above the liquidus temperature

$$\gamma(T) = (-4.102 \cdot 10^{-4}\ K^{-1} \cdot T + 2.51)\ \mathrm{N\ m^{-1}}. \quad (1)$$

Table 2 Constant material parameters of stainless steel 1.4301 computed with JMatPro.

Material parameter		Quantity	Unit
Density	ρ	7026	$\mathrm{kg\ m^{-3}}$
Kinematic viscosity	ν	7.158	$\mathrm{mPa\ s^{-1}}$
Specific heat capacity	c_p	804	$\mathrm{J\ kg^{-1}\ K^{-1}}$
Thermal conductivity	λ	31.531	$\mathrm{W\ K^{-1}\ m^{-1}}$
Thermal diffusivity	α	5.582	$\mathrm{mm^2\ s^{-1}}$
Latent heat	L_c	171.401	$\mathrm{kJ\ kg^{-1}}$

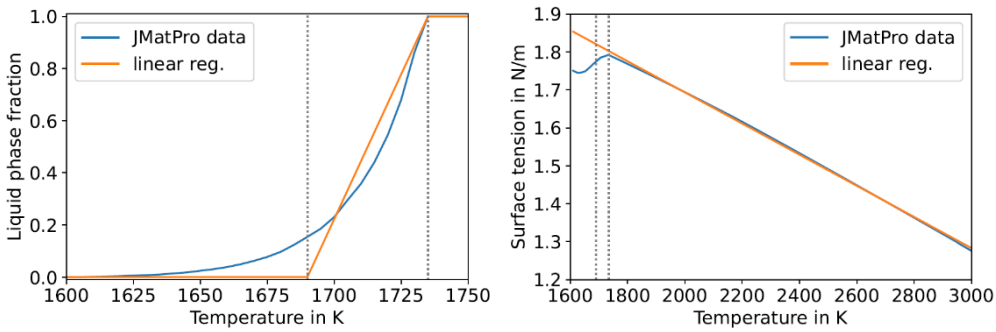

Fig. 1 Temperature dependent material parameters of stainless steel 1.4301 used in the simulation (orange) compared against the data from JMatPro. The two dashed lines indicate temperature solidus and liquidus used in the simulations.

EXPERIMENT

In-situ synchrotron X-ray imaging of the LBW process zone was conducted at the P07 (EH4) high-energy beamline at PETRA III, DESY (Hamburg, Germany) [27]. A schematic illustration of the experimental setup is shown in Fig. 2. The X-ray imaging system's core components included the DESY synchrotron (X-ray source), a scintillator, and a high-speed camera. The synchrotron X-ray beam, with a 2×2 mm^2 cross-section, irradiated samples (dimensions: $100 \times 30 \times 2$ mm^3) at the process zone. X-ray attenuation within the workpiece is dependent on material density; consequently, the gas-filled keyhole and the liquid melt pool exhibit lower attenuation than the solid material, which leads to different X-ray intensities after the sample. The transmitted and attenuated X-ray beam was converted into visible light by a 1.2 mm thick Cer-doped Gadolinium Aluminum Gallium Garnet (GaGG:Ce) scintillator, positioned approximately 3.5 m after the sample. An i-SPEED 727 high-speed camera (iX Cameras), equipped with a magnification lens, captured the intrinsic luminescence from the scintillator's backside. For these investigations, the beamline operated at a photon energy of 74 keV, and videos were recorded at a resolution of 1600×900 pixels with a frame rate of 7500 frames s−1. The raw data was further processed to improve the quality according to Forster et al. [15].

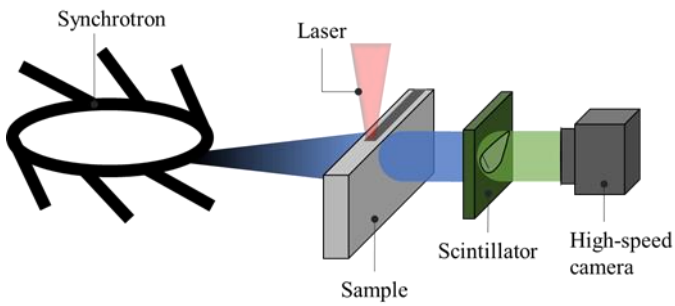

Fig. 2 Schematic illustration of the experimental setup. Reprinted from [15] under the CC BY-NC-ND 4.0 license

The LBW system featured a Trumpf TruDisk 8001 disc laser with a wavelength of 1030 nm, a 100 μm core diameter fiber optic cable (Newson NV, Dendermonde, Belgium), and a 2D galvanometer scanner system. A collimator lens ($f = 80$ nm) in combination with a f-theta focusing lens ($f = 163$ nm) provided a 1:2 magnification, resulting in a measured laser beam diameter of approximately 214 μm.

The specimens were mounted upright in a clamping device. Welding was carried out on the top edge of the sample. During the experiments, the sample remained stationary while the galvanometer scanner mirrors moved the laser beam at the desired feed rate. The feed rate was varied from 20 mm s−1 to 200 mm s−1, while the laser power ranged from 500 W to 1500 W. A compressed-air cross-jet was employed to protect the welding optics from spatter and metal fumes.

The temperature at the edge of the keyhole was measured using a hyperspectral camera [28]. The measurements showed temperatures between 2700 K and 2900 K during the process. The temperature fluctuations are due to process instabilities.

SIMULATION WITH KISSAM

The KiSSAM[2] [29] software framework is employed for high-fidelity simulation of the experimental LBW process. KiSSAM provides a detailed and physically comprehensive representation of melt pool dynamics. In previous studies, KiSSAM has been applied to a variety of additive manufacturing problems, including finding optimal parameters of single tracks [30], wetting effects on melt morphology [31], and increased layer thickness strategies in powder bed fusion [32]. In this work, KiSSAM is used as a reference to assess the validity and limitations of the underlying physical effects [29, 33].

KiSSAM explicitly models the gas-liquid interface using a volume-of-fluid (VOF) approach. This enables dynamic evolution of the keyhole shape under the influence of recoil pressure, surface tension, and evaporation-induced mass loss. The hydrodynamics solver is based on a weakly compressible lattice Boltzmann method (LBM) using a D3Q27 stencil. In contrast to macroscopic discretizations of the governing equations, the LBM employs a mesoscopic formulation based on particle distribution functions, which recover the Navier-Stokes equations in the low-Mach-number regime [34]. Hydrodynamics are restricted to the molten region. Heat transfer and phase change are modeled via an enthalpy-based formulation. The laser energy input is computed via ray tracing, accounting for multiple reflections within the keyhole cavity. This physical coupling - alongside modeling of surface tension (including Marangoni effects), strong evaporation and bubbles tracking - allows the simulation of keyhole collapse, bubble formation, and melt pool oscillations. No empirical fitting parameters are introduced; all phenomena are derived from fundamental physics. The only physics that is neglected is the vapor gas dynamics as well as the laser-vapor interactions.

KiSSAM employs dynamic mesh refinement and coarsening around the melt pool to keep correct simulation of the whole sample welded plate while minimizing computational cost in the surrounding solid material. The material domain is split into regions with distinct resolution levels, and the solver operates with high efficiency due to full GPU parallelization and a single-precision numerical implementation.

SIMULATION WITH WALBERLA

A second numerical model is implemented within the high-performance multiphysics framework WALBERLA [35, 36] combined with the pycodegen[3] family of Python-packages

[2] www.kissam.cloud
[3] pycodegen.pages.i10git.cs.fau.de

for scientific code generation. While KiSSAM aims at a detailed representation of dynamic keyhole formation and melt pool evolution, the WALBERLA-based approach follows a deliberately reduced modeling strategy. Its primary purpose is to investigate the melt pool response under controlled thermal and pressure boundary conditions, thereby enabling a systematic assessment of the influence of keyhole-related assumptions.

The melt pool dynamics are described by the incompressible Navier-Stokes equations and solved using the LBM on a D3Q19 stencil. Phase change between liquid and solid is modeled using the Partially Saturated Method (PSM) [37]. The solid fraction is introduced as a continuous variable defined between solidus and liquidus temperature. In this formulation, the mushy zone is treated as a hydrodynamic damping region: as the solid fraction increases during solidification, melt flow is progressively reduced until motion ceases in the fully solid state. The transition from liquid to solid is therefore represented as a continuous reduction of flow mobility. The model does not account for mechanical stiffness of the solid, volumetric shrinkage, microsegregation, feeding of the mushy zone, or stress evolution during solidification. The influence of the solidifying region on the melt pool is thus limited to hydrodynamic damping and thermal transport.

Thermal transport is modeled using a passive-scalar LBM formulation [38, 39]. The temperature field is tightly coupled to the melt flow and evolves according to convective and diffusive heat transport. Phase change is incorporated using an enthalpy-based approach, in which latent heat effects are accounted for within the energy balance. The local temperature is obtained from the specific enthalpy, considering both sensible heat and latent heat contributions, based on the material properties defined in Section 2.1. This formulation ensures thermodynamic consistency between heat transfer and solidification.

In contrast to KiSSAM, the WALBERLA model does not explicitly resolve evaporation dynamics, recoil pressure formation, or laser energy absorption within the keyhole. Instead, these complex processes are represented implicitly through prescribed boundary conditions at the keyhole surface. Therefore, the keyhole geometry is defined as a fixed spherocylindrical cavity with dimensions comparable to the experimentally observed keyhole. This simplification eliminates the explicit modeling of evaporation-driven interface deformation and gas-phase dynamics.

Laser energy deposition is represented by imposing a constant Dirichlet boundary condition of 2700 K at the keyhole surface, corresponding to the experimentally measured temperature range. In addition, a depth-dependent pressure boundary condition is applied along the keyhole wall to approximate the effect of evaporation-induced recoil pressure. Free-slip conditions are enforced tangentially at the cavity surface, allowing unimpeded melt flow along the interface while preventing normal penetration.

The imposed temperature and pressure distributions are thus implanted rather than computed from first principles. By prescribing these thermodynamic conditions directly at the cavity interface, the model deliberately bypasses detailed laser-matter interaction and evaporation-induced energy losses. The WALBERLA simulations should therefore be interpreted as a controlled numerical study of boundary-condition effects on melt pool flow and geometry rather than as a fully predictive description of the laser-material interaction.

The numerical implementation leverages WALBERLA's block-structured domain decomposition and MPI-based parallelization combined with GPU acceleration. The LBM

kernels are generated automatically using the code-generation frameworks pystencils [40, 41] and lbmpy [42-44], which translate symbolic descriptions of the governing equations into optimized C++/CUDA code at build time. This approach ensures performance portability while enabling rapid modification of physical models and boundary conditions.

A more detailed description of the mathematical formulation, the specific lattice Boltzmann schemes, and the implementation details of the waLBerla simulation and the used models can be found in Appendix.

MODELING ASSUMPTIONS

It is important to emphasize that both modeling frameworks focus exclusively on the thermo-fluid dynamics of the melt pool. Gas-phase dynamics, thermomechanical coupling, volumetric shrinkage, and stress evolution during solidification are not considered. Consequently, the simulations capture heat and mass transport, but they do not directly predict crack initiation or propagation. While solidification velocity and temperature gradients constitute necessary input parameters for solidification cracking models, the connection to cracking is therefore indirect. Within the research unit FOR5134[4], the computed solidification conditions are provided to complementary subprojects that specifically address the mechanisms and prediction of solidification cracks in an integrated, multi-scale framework.

Both simulation approaches rely on several assumptions, namely, treating the melt as incompressible, representing the transition from liquid to solid as a continuous variation of the local solid fraction between solidus and liquidus temperatures, and neglecting energy absorption and momentum transfer by the vapor phase.

Two complementary simulation strategies are employed. KiSSAM resolves the dynamic evolution of the keyhole, explicitly tracking the gas-liquid interface using a Volume-of-Fluid (VOF) approach. The keyhole geometry evolves under the influence of surface tension and recoil pressure. WALBERLA, in contrast, prescribes a fixed keyhole geometry, suitable for quasi-stationary conditions, allowing a systematic investigation of how boundary conditions influence steady-state melt pool flow.

Laser energy deposition is treated differently in the two models. KiSSAM accounts for multiple reflections within the keyhole using ray tracing, while WALBERLA applies a constant temperature boundary condition at the keyhole surface.

Stainless steel 1.4301 is used as a representative material to study melt pool dynamics during LBW, but it should be noted that phenomena such as evaporation and material properties, including temperature-dependent surface tension and solidification behavior, are highly sensitive to the specific alloy composition and welding conditions.

[4] https://www.for5134.science/en/

SIMULATION SETUP

Two LBW setups with power levels of 500 W and 1000 W and a feed rate of 100 mm s^{-1} were simulated. The spatial resolution was set to $\Delta x = 5$ µm in all cases. The time step sizes were $\Delta t = 75$ ns for the KiSSAM simulations and $\Delta t = 100$ ns for the WALBERLA simulations. The finest mesh size surrounding the melt pool in the KiSSAM simulations for a fully developed melt pool is 1.1×0.6 mm^2 in x and y-direction and 1.4 mm or 2.4 mm for 500 W and 1000 W in z-direction, respectively. For WALBERLA, both settings used a domain size of 4×2 mm^2 in x and y-direction and 1 mm or 2 mm for 500 W and 1000 W in z-direction, respectively. In KiSSAM, the laser moves according to the feed rate and the keyhole develops due to laser absorption and evaporation pressure. In contrast, the keyhole in WALBERLA simulations is geometrically fixed. The keyhole shape is modelled with a spherocylinder [45], consisting of a cylinder and an ending hemisphere with a total depth of 0.66 mm and 1.3 mm for the 500 W and 1000W respectively (diameter similar to the beam diameter). The laser movement is modeled implicitly by shifting the fluid velocity field by the laser's feed rate prior to its use in the thermal update, effectively transitioning to a co-moving reference frame. On the keyhole surface, a constant Dirichlet boundary condition with 2700 K according to the measurements is applied. In addition, a free-slip condition in combination with a pressure gradient is applied to the fluid field permitting unimpeded tangential flow near the keyhole and enabling different pressures inside the keyhole. The additional pressure is linearly increased from zero at the top to 176 kPa at the bottom end of the keyhole shape. The motivation for this choice is the assumption, that on the horizontal walls of the keyhole, the evaporation pressure keeps the keyhole open, and no other major pressures are acting. At the bottom, a significant acceleration occurs, which is well seen during bubble escape. Therefore, a pressure near the evaporation pressure for this material at 2700 K is chosen [46].

The whole domain is initialized at room temperature. KiSSAM uses Dirichlet boundary conditions at the domain boundaries at room temperature accordingly. It further applies no-slip boundary conditions between the melt pool and the solid material as well as pressure boundary conditions incorporating wetting, surface tension, Marangoni and evaporation pressure at the free surface between the melt pool and the atmosphere. WALBERLA applies free-slip boundary conditions for both LBM solvers at the top and bottom domain boundaries, which impose symmetry with respect to the wall-normal direction. On the horizontal boundaries, WALBERLA uses Dirichlet boundary conditions at room temperature. The corresponding fluid boundaries are treated the PSM.

RESULTS

EXPERIMENT

Utilizing high-speed synchrotron X-ray imaging, the real-time dynamics of the laser welding process, specifically the formation and evolution of the keyhole and melt pool, were directly observed. As shown in Fig. 3, a series of four representative frames were extracted of a video sequence[5] for a beam power of 1000 W.

The keyhole and melt pool appear brighter in the images compared to the solid material, a result of their lower density and consequently reduced X-ray absorption. At the top of the image, a darker region is visible, representing the resolidified or still molten weld seam surface. For enhanced clarity, the melt pool is delineated with a white dotted line. Due to the phase contrast enhancement inherent in the imaging technique, changes in the refractive index at the keyhole and melt pool boundaries are visualized as a black line. Fig. 3a shows the initial evolution of the keyhole. In Fig. 3b, the keyhole has deepened, and a small melt pool has formed on the side opposite the feed direction. By Fig. 3c, the keyhole has reached its maximum depth, while the melt pool has expanded but is not yet fully developed. Finally, Fig. 3d illustrates the fully developed melt pool with a depth of approximately 1.3 mm, along with the onset of keyhole pore strangulation. These start as bubbles, escaping from the keyhole and being transported within the melt pool flow, exhibiting mean velocities of approximately 0.1 m/s to 1 m/s. Additional measurements indicate that the surface temperature specifically at the keyhole area of the melt pool reaches approximately 2700 K.

[5] https://www.for5134.science/en/teilprojekte/thermo-fluiddynamische-untersuchung/

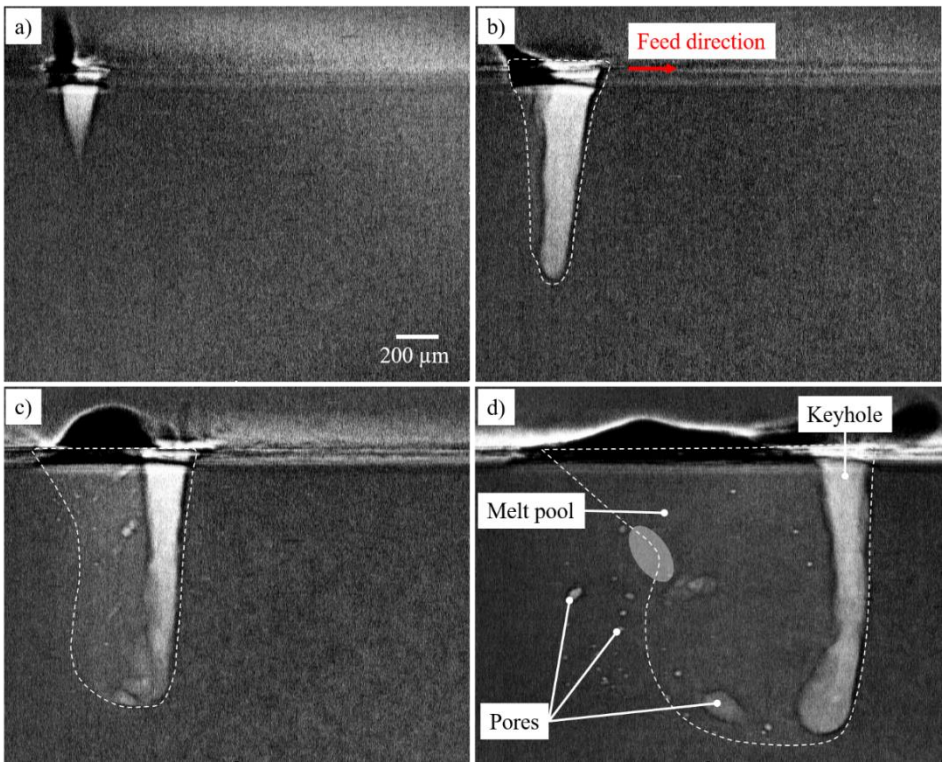

Fig. 3 X-ray images from laser welding with 1000 W. a) Insertion of the laser into the material, keyhole formation after 0.27 ms; b) Deepening of the keyhole and melt pool formation after 1.2 ms; c) Final keyhole depth after 4.3 ms; d) Fully developed keyhole and melt pool after 11.5 ms. Area of uncertainty regarding the melt pool shape is highlighted in light gray.

SIMULATION

The results from KiSSAM and WALBERLA are provided for a power of 1000 W. The simulation results are compared via 3D representations of the melt pool and the melt pool velocity in Fig. 4.

In both subfigures, the volume +/- 50 µm in y direction around the center of the simulation domain is shown. The melt pool dynamics are visualized by streamlines of the melt pool with the velocity magnitude represented by color from violet to yellow. The melt pool shape is approximated by the solidus and liquidus isotherms. In the KiSSAM results, the dynamically developed keyhole is determined by a contour surface at a fill level of 50 %. The static, cylindrical keyhole of the WALBERLA simulation is illustrated in red color.

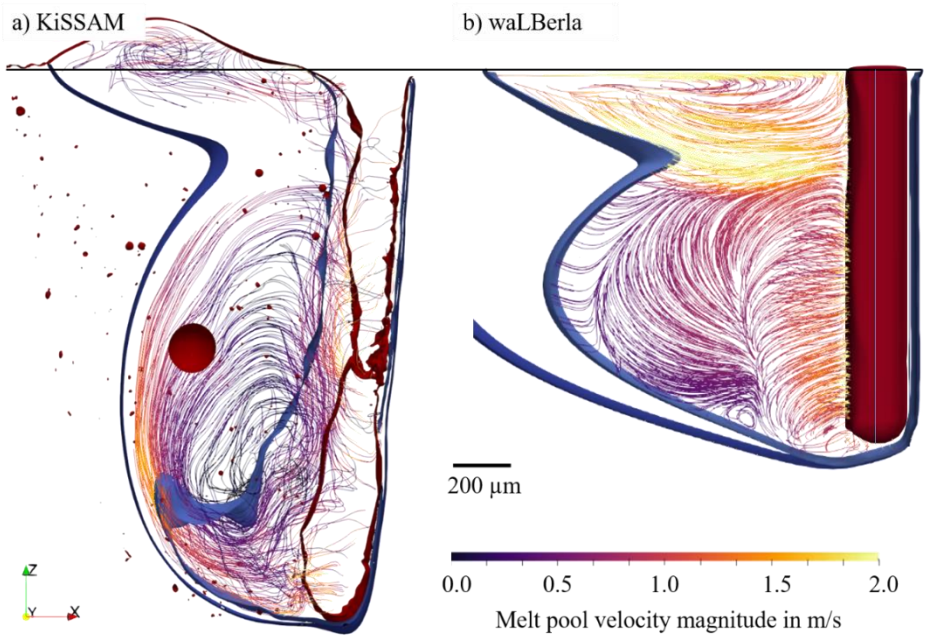

Fig. 4 Comparison of melt pool shape (represented by the solidus and liquidus isotherms in blue) and velocities via colored streamlines for 1000 W of a) KiSSAM and b) waLBerla. The keyhole is represented as red isosurface.

Simulation with KiSSAM

The simulation results from KiSSAM show a dynamically evolving keyhole and melt pool shape (see Fig. 5 and movie in supplementary material). The liquid melt pool is visualized in blue by the solidus and liquidus isotherms. For comparison, the simulation results are superimposed on the experimental results from Fig. 3.

The laser drills rapidly into the material by pushing the liquid melt out of the keyhole (see Fig. 5a+b). After approximately 1.5 ms the keyhole has a depth of 1.3 mm. The numerical melt pool evolves similar to the experimental observations albeit with a time shift of a few microseconds. The quasi steady state of the keyhole in Fig. 5d is much higher than in the experiment with a depth of appropriately 2 mm, which is discussed in Section 4. The keyhole shape is slightly tilted due to the laser movement. In addition, the keyhole shows an irregular surface. During welding, parts of the melt pool start to drop into the keyhole and in the laser path. Due to a subsequent high laser absorption, this material is directly pushed back into the melt pool. At the bottom of the keyhole, some bubbles escape from the keyhole, similar to the experiment. The melt pool dynamics show a circular vortex in the bottom half of the melt pool and some vertical movement in the upper part. A steady mean temperature over the whole keyhole of approximately 2450 K is established. This mean value is computed by averaging

the temperature of every interface cell at the volume-of-fluid boundary to the keyhole. In contrast, cell-local temperature peaks up to 6900 K are observed at specific points, where the laser is directly hitting the material; however, these peaks are excluded from the reported mean value to provide a more stable representative temperature of the keyhole walls.

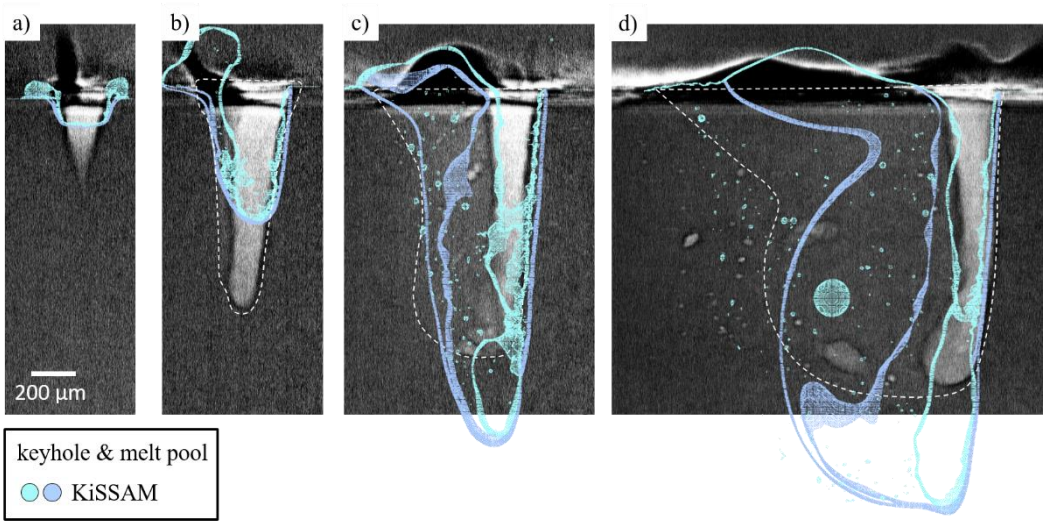

Fig. 5 X-ray images from Fig. 3 superimposed with KiSSAM simulation results (contour of keyhole in cyan as well as solidus and liquidus isotherms in blue representing the melt pool) at similar times: a) 0.27 ms, b) 1.2 ms, c) 4.3 ms and d) 11.5 ms.

Simulation with waLBerla

Due to the fixed keyhole geometry for the waLBerla simulation, only the steady state is presented in Fig. 5. The final melt pool depth is 1.4 mm, which is only slightly larger than the keyhole itself. Two recirculation zones are obvious. At the top of melt pool there is a fast recirculation zone dominated by the Marangoni effect driven by the surface tension. The second recirculation zone with fast melt pool velocities is observed due to the keyhole forces acting at the bottom of the keyhole. These two eddies lead to a double recirculation zone in the top-middle of the melt pool with low melt pool velocities. Due to the PSM method, the melt pool velocities in the mushy zone between the liquidus and solidus isotherm are almost zero. A remarkable kink is visible in the liquidus isotherm, which is a result of the underlying melt pool dynamics.

Performance

The computation time for both simulation tools was tracked for two different beam powers of 500 W and 1000 W. A direct performance comparison between the simulation frameworks is not feasible due to fundamental differences in their modeling scope and numerical configurations. Specifically, the two applications differ in physical complexity, LBM stencil choices, numerical precision (single vs. double), and the hardware architectures on which the simulations were executed. These discrepancies preclude a fair and meaningful evaluation of absolute performance metrics such as runtime or throughput.

Despite its high physical and computational complexity, KiSSAM is executed on a single RTX 3090 GPU. The software achieves a total simulation time of the last 7.5 ms (100,000 time steps) for 500 W (approx. 8 million cells) of 1.96 h and for 1000 W (approx. 12 million cells) of 2.99 h, respectively. This outstanding performance is realized by optimized GPU code and mesh refinement surrounding the melt pool. In addition, the advantages of the RTX 3900 are used due to the single-precision execution of the simulation.

In the present state, the grid refinement of waLBerla could not be used here. Therefore, the simulations are executed on 8 NVIDIA A100 GPUs. The software achieves a total simulation time for 30 ms real time (500,000 time steps) for 500 W (approx. 64 million cells) of 1.5 h and for 1000 W (approx. 128 million cells) of 3 h, respectively. The total simulation time is comparable with KiSSAM, although less physical phenomena are tracked. Possible performance improvements are achievable by grid refinement and by replacing double with single precision computations.

DISCUSSION

MELT POOL EVOLUTION

The experimentally observed evolution of the melt pool is slightly underestimated by the KiSSAM simulation (see Fig. 5a+b) within the first milliseconds. Here, the melt pool dynamics are mainly driven by the evaporation pressure. KiSSAM underpins, that the covered physics including laser beam ray-tracing, absorption and multi-reflection as well as the hydro- and thermodynamical models are suitable to describe this stage of melting, although there is a small shift in time of a few microseconds until the correct melt pool depth is reached. One reason is the coarse cell size of the finest mesh of 5 µm. With a finer cell size, this effect gets less significant. These results are similar to additive manufacturing examples [30-32], where the melt pool depth is normally smaller than 1 mm. In addition, the initial evolution of the melt pool is of less importance than the quasi-stationary state for welding and additive manufacturing processes.

However, Fig. 5c+d clearly show that the numerical prediction significantly overestimates the melt pool depth once approaching the quasi-stationary state. Consequently, the overall shape of the melt pool does not match the experimental observations. The upper vortex, driven by the Marangoni effect, is considerably smaller than in the experiment and in a low temperature range between solidus and liquidus temperature. In addition, the keyhole walls exhibit stronger instabilities.

In the current KiSSAM simulations, the keyhole walls absorb only minor fractions of laser energy, primarily through multi-reflections. Unless material intrudes into the laser channel, the walls remain comparatively cold. This is consistent with the simulated mean wall temperature of approximately 2450 K, which is significantly lower than the experimentally measured average temperature of about 2700 K. If material enters the beam path, it is rapidly heated and expelled, leading to localized and intermittent heating events. This mechanism results in unsteady melt pool dynamics, reflected by the zig-zag pattern of the temperature isolines (Fig. 5d).

Although KiSSAM has demonstrated high predictive capability for similar processes with different materials under specific parameter sets, the present discrepancies indicate that additional physical mechanisms may be missing. The absence of explicit vapor-phase modeling has two distinct implications. First, the stabilizing vapor pressure inside the keyhole is not resolved. In reality, the metal vapor exerts a distributed pressure along the keyhole walls, counteracting surface tension and hydrostatic forces and thereby contributing to geometric stability. Without this vapor pressure contribution, the simulated keyhole is more susceptible to local wall instabilities and collapse events. Second, laser absorption within the vapor phase is not considered. If a significant fraction of the laser energy is absorbed by the metal vapor before reaching the melt pool bottom, the energy input into the deeper regions of the cavity would be reduced. This would directly influence the melt pool depth and the overall penetration behavior. The overestimation of melt pool depth in the present simulations therefore likely results primarily from the absence of vapor-phase absorption rather than from missing pressure effects alone. Trapp et al. measured the absorptivity of stainless steel SS316L

during keyhole welding and conclude a value of approximately 78 % [47]. In contrast, the energy absorption due to multi-reflection in KiSSAM simulations is almost 100 %. Assuming a significant absorption of the metal vapor inside the keyhole, the melt pool shape and dynamics will change. The consequence is that less laser energy is absorbed at the melt pool bottom, which results in a smaller melt pool depth and in total in less evaporation losses regarding energy and mass.

QUASI-STATIONARY STATE

A comparative analysis of all simulation results and the experiments for 500 W and 1000 W is presented in Fig. 6. The background displays experimental synchrotron imaging of the cross-section along the laser scanning direction. The keyhole region is highlighted in light gray, enclosed by a dashed contour that delineates the melt pool boundary. Superimposed on these experimental images are the simulation results: the KiSSAM iso-surfaces are depicted as light blue wireframes, while the WALBERLA simulation results are shown in green. This visual overlay enables a direct qualitative comparison of the quasi-stationary state between experimental observations and numerical predictions. The differences in the melt pool evolution between KiSSAM simulation and the experiments are already discussed in Section 4.1. Here, it is obvious that the described mechanism of overestimated evaporation is present for both powers. In contrast, the WALBERLA simulations can reproduce the overall shape and melt pool dynamics of the experiments. Because the keyhole and all boundary conditions do not change over time, a stationary state evolves. The vortices driven by evaporation and the Marangoni effect form the outer shape of the melt pool represented by the liquidus isolines. Both vortices lead to the formation of a kink in this isoline. The evaluation of the melt pool shape from the experiments, especially in this region, is not straight forward. Consequently, the dashed white line has a high uncertainty in this region. Summing up, the defined boundary condition results in a realistic melt pool shape.

It must be noted that the improved accuracy of the simplified waLBerla model does not imply a more complete physical description of the laser-matter interaction. The agreement with experimental melt pool geometries primarily highlights the strong sensitivity of the melt pool shape to the boundary conditions applied on the keyhole walls. By prescribing steady-state temperature and pressure distributions derived from experiments, the model enforces the dominant thermodynamic driving forces in a controlled manner, which enhances numerical robustness within a specific regime. However, this approach does not resolve the dynamic evolution of the keyhole, transient evaporation processes, or vapor-induced energy losses. A fully predictive model must ultimately incorporate these coupled and time-dependent mechanisms.

For a quantitative comparison, the melt pool cross section area and volume are evaluated for both simulation tools (see Table 3). The melt pool volume predicted by KiSSAM is approximately a factor of four smaller than that of the WALBERLA simulation. Similarly, the cross-sectional area of the melt pool in the KiSSAM results is reduced by roughly a factor of two. Moreover, in KiSSAM, the average melt pool temperature is lower, with a substantial fraction of the melt pool residing in the mushy zone, which is not observed in the WALBERLA

simulations. These results support the assumption of overestimated evaporation at the melt pool bottom for the KiSSAM simulation. The highly localized absorption of the laser energy results in extreme surface temperatures within individual computational cells of up to 6900 K and consequently to very high evaporation losses in terms of both energy and mass. In this context, 'local' refers specifically to the temperature of a single cell at the point of laser interaction rather than a region-wide average. As a result, insufficient energy remains within the liquid melt pool. Although the melt pool is deeper, the total volume is too small. It should be emphasized that an explicit modeling of gas-phase flow, recondensation effects, or vapor superheating alone would not fundamentally alter this penetration behavior. While such effects could redistribute energy locally and potentially increase the overall melt pool volume, they would not significantly reduce the penetration depth. A reduction in melt pool depth requires that less laser energy reaches the keyhole bottom. This can only occur if a portion of the laser radiation is absorbed within the metal vapor before interacting with the melted surface. This comparison therefore strengthens the hypothesis that absorption of the laser beam within the vapor phase inside the keyhole plays a decisive role in determining melt pool depth and total evaporation losses.

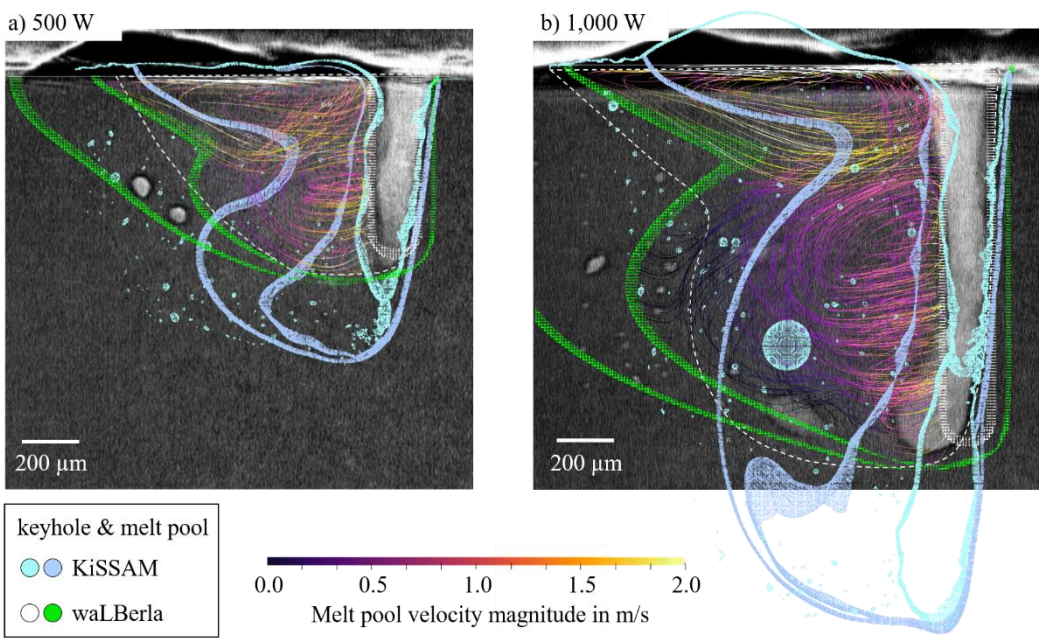

Fig. 6 Comparison between experiment (keyhole shown in gray), KiSSAM (shades of cyan) and waLBerla (green) simulation results regarding keyhole and melt pool shape (represented by solidus and liquidus isotherms). Additionally fluid velocities inside the pure liquid melt pool are visualized via colored streamlines.

Table 3 Melt pool evaluations for KiSSAM and waLBerla simulation results.

Energy Input	500 W		1000 W	
Software tool	KiSSAM	waLBerla	KiSSAM	waLBerla
Cross section	0.47 mm²	0.96 mm²	0.96 mm²	2.49 mm²
Volume	0.05 mm³	0.20 mm³	0.13 mm³	0.52 mm³

To reflect this change in absorption, the KiSSAM simulations were repeated with the beam power reduced to 80 % after 1.2 ms, once the keyhole has evolved. The results of both simulations are compared to the experimental observations in Fig. 7. As expected, the melt pool reaches now a reasonable depth. However, the unsteadiness of the keyhole walls as well as the underestimated extend of the Marangoni-driven flow region is almost unaffected. This indicates that the simplified treatment of the vapor phase is insufficient to reproduce the experimentally observed stabilization mechanisms. In particular, the absence of an explicit gas-phase model prevents a physically consistent description of vapor pressure and its stabilizing effect on the keyhole, which limits the agreement between simulation and experiment. These topics are addressed in future work.

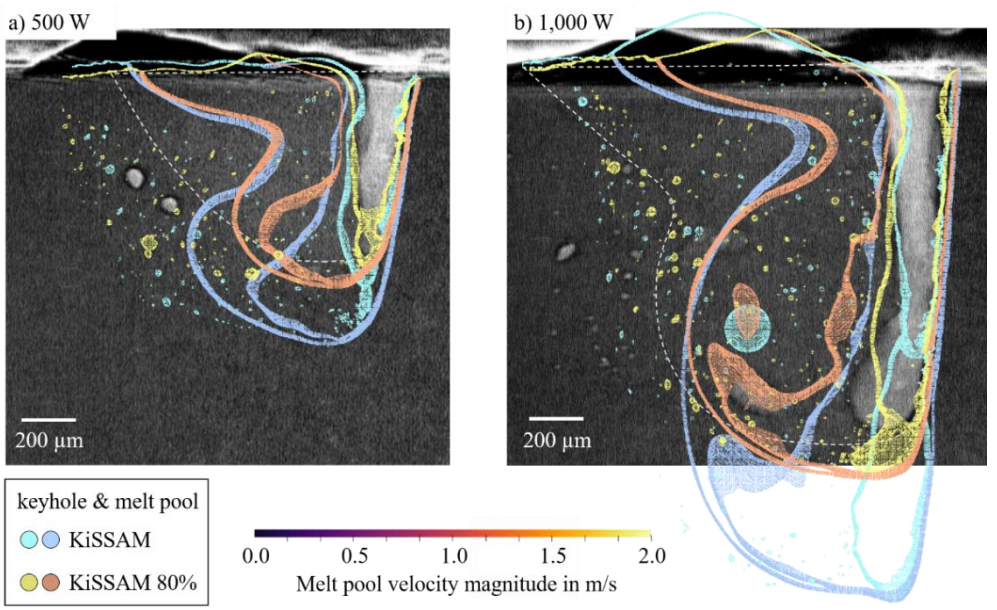

Fig. 7 The experimental data show the keyhole as a light-gray background region, with the melt-pool geometry indicated by a dashed line. These measurements are compared with the KiSSAM simulations at 80 % beam power, shown in orange and yellow, and at 100 % beam power, shown in blue and cyan, using the solidus, liquidus, and keyhole isotherms for a) 500 W and b) 1000 W.

CONCLUSION AND OUTLOOK

This work presented experimental and numerical investigations of LBW of stainless steel 1.4301 for two parameter sets in the deep penetration regime. Both simulation frameworks are capable of resolving several microseconds of process time within a few hours on modern GPU architectures. The study focused exclusively on the thermo-fluid dynamics of the melt pool and keyhole. Solidification cracking itself was not modeled directly; instead, solidification velocities and temperature gradients are easy to be extracted to serve as input for complementary mechanical computations.

The comparison between synchrotron experiments and simulations revealed that the transient melt pool evolution is well captured by the state-of-the-art tool KiSSAM. However, significant deviations arise in the quasi-stationary regime. In particular, melt pool depth, keyhole stability, and flow topology cannot be reproduced satisfactorily when the gas phase as well as laser–vapor interaction are neglected.

Using a reduced modeling approach implemented in waLBerla, the experimentally observed melt pool shape could be reproduced by imposing more homogeneous temperature and pressure boundary conditions at the keyhole interface. This comparison leads to two central conclusions.

First, our results confirm previous findings from the literature that the gas phase cannot be neglected in deep-penetration laser welding. For numerical simulations, its presence significantly influences pressure and temperature distributions inside the keyhole, which in turn affect melt pool geometry, flow behavior, and cavity stability.

Second, modeling the gas phase alone is insufficient. Absorption of laser radiation within the metal vapor must be considered to correctly predict the redistribution of energy inside the keyhole. Only a reduction of laser intensity reaching the keyhole bottom can consistently explain the experimentally observed penetration depth. Vapor-phase absorption further influences keyhole stability and characteristic geometric features. The present results therefore indicate that accurate prediction of quasi-stationary keyhole regimes requires a physically consistent coupling of melt flow, vapor pressure effects, and laser-vapor energy interaction.

It should be emphasized that the conclusions drawn here are regime-specific and based on a single alloy investigated under two parameter sets. Since evaporation behavior, surface tension characteristics, and keyhole dynamics are strongly alloy- and process-dependent, broader validation across different materials and welding conditions is required before generalization.

Future work will therefore focus on three directions. First, dedicated experimental investigations will quantify laser absorption and diffraction within the metal vapor inside the keyhole. Second, these experimentally derived absorption models will be integrated into KiSSAM, including explicit vapor-phase modeling and improved ray-tracing approaches. Third, the waLBerla framework will be extended by adaptive grid refinement and single-precision optimization to further enhance computational efficiency while preserving physical fidelity.

CREDIT AUTHORSHIP CONTRIBUTION STATEMENT

J. Plewinski: Data curation, Formal analysis, Investigation, Methodology, Software, Validation, Visualization, Writing – original draft, Writing – editing; F. Hennig: Software, Writing - original draft; C. Forster: Data curation, Investigation, Validation, Visualization, Writing - original draft; S. Belousov, A. Zakirov, B: Korneev: Investigation, Software, Writing - original draft; C. Spurk, M. Hummel, A. Olowinsky, F. Beckmann, J. Moosmann: Investigation, Resources; M. Schmidt, H. Köstler: Funding acquisition, Project administration, Resources, Supervision, Writing - review and editing; M. Markl: Conceptualization, Funding acquisition, Methodology, Project administration, Software, Supervision, Validation, Visualization, Writing – original draft, Writing - review and editing

DECLARATION OF GENERATIVE AI AND AI-ASSISTED TECHNOLOGIES IN THE WRITING PROCESS

During the preparation of this work the author(s) used OpenAI's ChatGPT (GPT-5-mini) in order to correct the English grammar. After using this tool/service, the author(s) reviewed and edited the content as needed and take(s) full responsibility for the content of the publication.

DECLARATION OF COMPETING INTEREST

The authors declare that they have no known competing financial interests or personal relationships that could have appeared to influence the work reported in this paper.

ACKNOWLEDGEMENTS

This study was funded by the Deutsche Forschungsgemeinschaft e.V. (DFG, German Research Foundation) and carried out within the framework of Research Unit FOR-5134, "Solidification Cracks during Laser Beam Welding: High Performance Computing for High Performance Processing", (Grant No. 434946896). The sponsorship and support are gratefully acknowledged.

The authors gratefully acknowledge the scientific support and HPC resources provided by the Erlangen National High Performance Computing Center (NHR@FAU) of the Friedrich-Alexander-Universität Erlangen-Nürnberg (FAU). The hardware is funded by the German Research Foundation (DFG).

The presented investigations were carried out within the cooperation "Laser Meets Synchrotron" (www.laser-meets-synchrotron.de). The experimental setup and its operation were funded by the Deutsche Forschungsgemeinschaft e.V. (DFG, German Research Foundation) within the framework of the Collaborative Research Centre SFB1120-236616214

“Bauteilpräzision durch Beherrschung von Schmelze und Erstarrung in Produktionsprozessen”. The experiments were carried out in cooperation with Helmholtz-Zentrum Hereon in Hamburg at Beamline P07 of DESY PETRA III as part of proposal BAG-20211050 and we would like to thank F. Beckmann, J. Moosmann and all people involved for their support. Support from the Erlangen Graduate School in Advanced Optical Technologies (SAOT) by the Bavarian State Ministry for Science and Art is also gratefully acknowledged.

Open access funding enabled and organized by Projekt DEAL.

APPENDIX A: IMPLEMENTATION-DETAILS OF WALBERLA

The second simulation tool is developed on the basis of the high-performance simulation framework WALBERLA combined with the pycodegen family of Python-packages for scientific code generation. WALBERLA [35, 36] is a versatile framework for massively parallel multi-physics simulations. Combining MPI-based distributed memory parallelism with either OpenMP, CUDA, or HIP, it was shown to achieve excellent performance and scalability across a range of applications [48-51].

In this work, two LBM schemes for the hydrodynamics of the melt pool and the overall thermodynamics in the material are combined. In addition, the physical effects of laser absorption, evaporation and Marangoni convection are accounted for by appropriate boundary conditions.

MELT POOL DYNAMICS

The melt pool dynamics in LBW is essentially described by the incompressible Navier-Stokes equations. In contrast to conventional macroscopic approaches, which discretize these equations directly, the LBM used here uses a mesoscopic description of the melt pool. The LBM is based on the discretization of the Boltzmann equation [34]. The basic equation

$$f_i(\boldsymbol{x} + c_i \Delta t, t + \Delta t) = f_i(\boldsymbol{x}, t) + \Omega_i(\nu, \boldsymbol{x}, t) + F_i(\boldsymbol{x}, t) \tag{2}$$

describes the temporal development of the particle distribution function (PDF) f_i at a grid point $\boldsymbol{x}$ at a time t. The discrete velocities c_i of the selected lattice model are defined so that the distance from one point in the grid to the next can be covered within one time step Δt. F_i represents an external force and Ω_i describes the collision operator. The collision operator relaxes the distribution functions towards an equilibrium according to the kinematic viscosity ν. The macroscopic quantities density ρ and velocity $\boldsymbol{u}$ can be calculated from the distribution functions f_i

$$\rho(\boldsymbol{x}, t) = \sum_i f_i\,(\boldsymbol{x}, t) \qquad\qquad \rho \boldsymbol{u}(\boldsymbol{x}, t) = \sum_i c_i f_i(\boldsymbol{x}, t) \tag{3}$$

A Chapman-Enskog analysis can be used to show that the LBM reproduces the incompressible Navier-Stokes equations in the limiting case of small Mach numbers [34].

Traditionally, the Navier-Stokes equation is applied only in the liquid melt pool. Therefore, a cell type parameter (liquid or solid) is introduced to distinguish whether the melt pool dynamics or a boundary condition is being calculated. The simplest boundary condition is a so-called bounce-back boundary condition, in which the distribution functions flowing into the solid cell are mirrored back to the liquid cell. This procedure corresponds to a no-slip boundary condition, i.e., the melt pool dynamics are entirely suppressed at the melt pool boundary. The bounce-back condition is typically implemented by an if-then-else condition in the innermost loop. This can lead to relatively slow execution speed and a large overhead on current GPU-based computer systems.

In this work, the LBM is extended with the PSM [37], such that the same computation can be performed uniformly without (slow) conditionals throughout the domain. The basic idea is to interpolate the collision operator Ω_i between the behavior of a liquid and a solid cell through the solid phase fraction of a cell. The modified collision operator is described by

$$\Omega_i(\nu, \boldsymbol{x}, t) = (1 - B)\Omega_i^{\mathrm{f}}(\nu, \boldsymbol{x}, t) + B\Omega_i^{\mathrm{s}}(\boldsymbol{x}, t) \tag{4}$$

with a weighting parameter $B \in [0; 1]$ that represents the solid phase fraction as a linear interpolation between T_{solidus} and T_{liquidus}. Ω_i^{f} describes the cumulant collision operator for the fluid cells [52], and Ω_i^{s} the solid collision operator given by

$$\Omega_i^s = \left(f_{\bar{\imath}}(\boldsymbol{x}, t) - f_{\bar{\imath}}^{eq}(\rho, \boldsymbol{u})\right) - \left(f_i(\boldsymbol{x}, t) - f_i^{eq}(\rho, \boldsymbol{u}_s)\right) \tag{5}$$

where $\boldsymbol{u}_s$ describes the velocity of the boundary at the local cell $\boldsymbol{x}$ and f_i^{eq} the equilibrium value [52]. A positive side effect of the PSM is that no more cell transformations are necessary, since the behavior is controlled by the solid phase fraction.

Free-slip boundaries impose symmetry with respect to the wall-normal direction. This is implemented by negating the PDFs corresponding to velocities normal to the boundary. In addition, no slip boundary conditions are established through the bounce-back method: PDFs streaming into the wall are reflected back into the domain, enforcing zero velocity at the wall. The surface tension force is computed from interfacial tension gradients along the interface that arise due to temperature-dependent variations (Marangoni effect), and is computed via

$$\boldsymbol{F}_{\mathrm{Marangoni}} = \nabla_s \gamma(T), \tag{6}$$

where ∇_s denotes the surface gradient operator and $\gamma(T)$ is the temperature-dependent surface tension.

THERMODYNAMICS

The conservation of energy is described by the heat conduction equation. This equation covers the entire energy balance, from heat sources, such as the absorption of the laser, to heat conduction through diffusion and heat sinks, such as evaporation losses. The passive scalar method, a special version of the LBM, is a numerical method to solve this equation [38, 39].

An additional set of distribution functions h_i is defined on the same grid, which is used for melt pool dynamics. These distribution functions are propagated analogously to f_i along discrete grid directions and brought into interaction with each other in a collision step

$$h_i(\boldsymbol{x} + c_i\Delta t, t + \Delta t) = h(\boldsymbol{x}, t) + (1 - \tau_h^{-1}\Delta t)\Phi_i(\boldsymbol{x}, t) \tag{7}$$

with

$$h(\boldsymbol{x}, t) = \frac{\sum_i f_i(\boldsymbol{x},t)h_i(\boldsymbol{x},t)}{\rho(\boldsymbol{x},t)} \quad . \tag{8}$$

Here, h_i represents the distribution function of the specific enthalpy h, τ_h the thermodynamic relaxation parameter and Φ_i the thermodynamic disequilibrium

$$\Phi_i(\boldsymbol{x}, t) = \frac{c_i - \boldsymbol{u}(\boldsymbol{x},t)}{\rho(\boldsymbol{x},t)c_s^2} \cdot \sum_j c_j f_j(\boldsymbol{x}, t) \Big(h_j(\boldsymbol{x}, t) - h(\boldsymbol{x}, t)\Big). \tag{9}$$

The hydrodynamic quantities ρ, $\boldsymbol{u}$ and f_j are taken directly from the LBM, whereby a coupling between melt pool dynamics and thermodynamics takes place. The thermal diffusivity α is related to the thermal relaxation time τ_h by $\alpha = (\tau_h - 0.5\Delta t)c_s^2$. The specific enthalpy h is converted into the temperature T by

$$T(\boldsymbol{x}, t) = \frac{h(\boldsymbol{x},t)/\rho(\boldsymbol{x},t) - L\big(h(\boldsymbol{x},t)\big)}{c_p} \tag{10}$$

where c_p describes the specific heat capacity, and $L(h)$ the latent heat, which is computed via

$$L\big(h(\boldsymbol{x}, t)\big) = \begin{cases} 0, & h \le h_{\text{solidus}} \\ L_c, & h \ge h_{\text{liquidus}} \\ L_c \frac{h(\boldsymbol{x},t) - h_{\text{solidus}}}{h_{\text{liquidus}} - h_{\text{solidus}}}, & \text{otherwise.} \end{cases} \tag{11}$$

Dirichlet boundary conditions are applied by directly setting all h_i in the respective boundary cells to values corresponding to the enthalpy derived from the target wall temperature. In addition, similar free-slip boundary conditions as for the melt pool dynamics are used.

A decisive advantage of the passive scalar method is its simple implementation and numerical efficiency. It can be based on the existing LBM infrastructure and benefits from its high parallelizability. Due to the regularized approach, the method exhibits improved stability and accuracy. In particular, energy conservation is ensured in contrast to other passive scalar methods, which is crucial for the simulation of thermal processes such as LBW.

IMPLEMENTATION

The application developed in this work computes in each time step the following steps:

1. Communication of all probability distribution functions (PDFs) f_i and h_i across process boundaries
2. Application of all boundary conditions at the outer boundaries of the simulation domain
3. Execution of thermodynamic LBM (Equation (7))
4. Computation and communication of temperature T
5. Application of keyhole pressure and surface tension forces
6. Execution melt pool dynamics LBM (Equation (2))

This approach enables a numerically efficient representation of LBW, capturing key effects such as melt pool convection, solidification, and surface-driven flows.

The implementation utilizes the distributed block-structured domain partitioning and field data structures provided by WALBERLA, as well as its MPI-based data synchronization engine. The described numerical schemes for melt pool dynamics and thermodynamics are implemented on a D3Q19 stencil by the domain-specific languages and code generation capabilities of pystencils [40, 41] and lbmpy [42-44]. The PSM is integrated into to the LBM using an algebraic procedure adapted from [53]. Further supporting operations, such as the computation of boundary conditions, are implemented entirely as symbolic equations. The numerical methods are defined in Python-scripts which are executed during the application build process. At that time, highly optimized target-specific implementations of the numerical kernels are automatically generated from their algebraic descriptions. Hiding the platform and optimization details inside the code generator ensures a significant level of hardware and performance portability. The code generation process is facilitated by a novel toolchain based on the metaprogramming tool pystencils-sfg[6]. Kernels, wrapped into classes adhering to the algorithmic idioms expected by WALBERLA, are thus emitted to C++ source files, which are then compiled alongside the conventionally programmed framweork. This process is illustrated in Fig. 8.

[6] i10git.cs.fau.de/pycodegen/pystencils-sfg

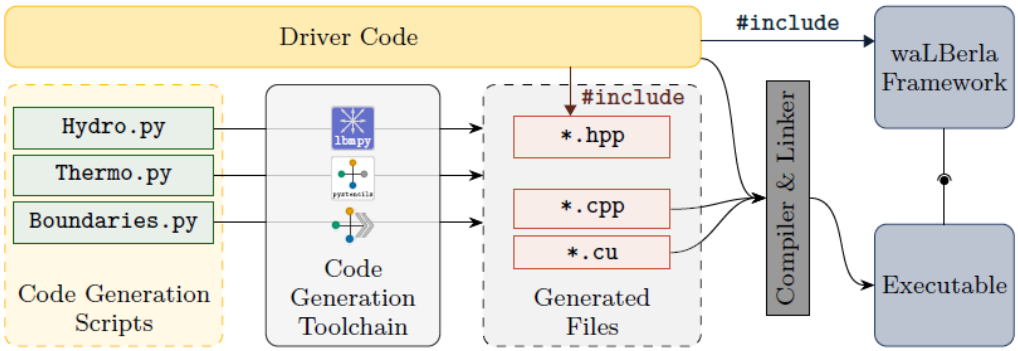

Fig. 8 Components and build flow of the waLBerla-based application

DATA AVAILABILITY

Data will be made available on request.

References

[1] A. KLIMPEL: 'Review and Analysis of Modern Laser Beam Welding Processes', *Materials* 17 (2024) 4657, https://doi.org/10.3390/ma17184657.

[2] W. PUMPHREY: 'A Consideration of the Nature of Brittleness at Temperatures Above the Solidus in Castings and Welds in Aluminium Alloys', *J. of the Inst. Of Metals* 75 (1948), 235-256.

[3] W. R. APBLETT, W. S. PELLINI: 'Factors which influence weld hot cracking', *Welding J. (N.Y.)* Vol: 33 (1954), https://www.osti.gov/biblio/4389407 (accessed August 27, 2025).

[4] J. C. BORLAND: 'Generalized theory of super-solidus cracking in welds', *Br. Weld. J.* 7 (1960), 508-512.

[5] N. PROKHOROV: 'Resistance to hot tearing of cast metals during solidification', *Russian Castings Production* 2.2 (1962), 172-175.

[6] K. ŁYCZKOWSKA, J. ADAMIEC: 'The Phenomena and Criteria Determining the Cracking Susceptibility of Repair Padding Welds of the Inconel 713C Nickel Alloy', *Materials* 15 (2022), 634. https://doi.org/10.3390/ma15020634.

[7] B. FOTOVVATI, S. WAYNE, G. LEWIS, E. ASADI: 'A Review on Melt-Pool Characteristics in Laser Welding of Metals', *Advances in Materials Science and Engineering* 2018 (2018), 1-18, https://doi.org/10.1155/2018/4920718.

[8] K. SCHRICKER, L. SCHMIDT, H. FRIEDMANN, C. DIEGEL, M. SEIBOLD, P. HELLWIG, F. FRÖHLICH, J. P. BERGMANN, F. NAGEL, P. KALLAGE, A. RACK, H. REQUARDT, Y. CHEN: 'Characterization of keyhole dynamics in laser welding of copper by means of high-speed synchrotron X-ray imaging', *Procedia CIRP* 111 (2022), 501-506, https://doi.org/10.1016/j.procir.2022.08.079.

[9] T. KLEIN, M. VICANEK, J. KROOS, I. DECKER, G. SIMON: 'Oscillations of the keyhole in penetration laser beam welding', *J. Phys. D: Appl. Phys.* 27 (1994) 2023, https://doi.org/10.1088/0022-3727/27/10/006.

[10] N. KOURAYTEM, X. LI, R. CUNNINGHAM, C. ZHAO, N. PARAB, T. SUN, A. D. ROLLETT, A. D. SPEAR, W. TAN: 'Effect of Laser-Matter Interaction on Molten Pool Flow and Keyhole Dynamics', *Phys. Rev. Appl.* 11 (2019), 064054, https://doi.org/10.1103/PhysRevApplied.11.064054.

[11] W. KURZ: 'Solidification Microstructure-Processing Maps: Theory and Application', *Advanced Engineering Materials* 3 (2001), 443-452, https://doi.org/10.1002/1527-2648(200107)3:7%3C443::AID-ADEM443%3E3.0.CO;2-W.

[12] F. KAUFMANN, C. FORSTER, M. HUMMEL, A. OLOWINSKY, F. BECKMANN, J. MOOSMANN, S. ROTH, M. SCHMIDT: 'Characterization of Vapor Capillary Geometry in Laser Beam Welding of Copper with 515 nm and 1030 nm Laser Beam Sources by Means of In Situ Synchrotron X-ray Imaging', *Metals* 13 (2023), 135, https://doi.org/10.3390/met13010135.

[13] M. HUMMEL, A. HÄUSLER, S. HOLLATZ, C. HAGENLOCHER, U. HALM, C. SCHÖLER, A. OLOWINSKY, A. GILLNER: 'Temporally and spatially highly resolved reconstruction of vapor capillary geometry during laser beam welding using synchrotron radiation', *Lasers in Manufacturing Conference* 2021, (2021).

[14] C. FORSTER, R. ROTHFELDER, P. KRAKHMALEV, C. SPURK, M. HUMMEL, A. OLOWINSKY, F. BECKMANN, J. MOOSMANN, M. SCHMIDT: 'Unveiling thermo-fluid dynamic phenomena in laser beam welding', *PAMM* 24 (2024), e202400194, https://doi.org/10.1002/pamm.202400194.

[15] C. FORSTER, M. DÖRING, C. SPURK, M. HUMMEL, A. OLOWINSKY, F. BECKMANN, J. MOOSMANN, M. SCHMIDT: 'In-situ observation of end crater crack mechanisms in AA7075 during laser beam welding using synchrotron radiation', *Procedia CIRP* 124 (2024), 464-467, https://doi.org/10.1016/j.procir.2024.08.154.

[16] Y. AI, P. JIANG, X. SHAO, P. LI, C. WANG: 'A three-dimensional numerical simulation model for weld characteristics analysis in fiber laser keyhole welding', *International Journal of Heat and Mass Transfer* 108 (2017), 614-626, https://doi.org/10.1016/j.ijheatmasstransfer.2016.12.034.

[17] Y. AI, P. JIANG, X. SHAO, P. LI, C. WANG, G. MI, S. GENG, Y. LIU, W. LIU: 'The prediction of the whole weld in fiber laser keyhole welding based on numerical simulation', *Applied Thermal Engineering* 113 (2017), 980-993, https://doi.org/10.1016/j.applthermaleng.2016.11.050.

[18] T. YU, J. ZHAO: 'Quantitative simulation of selective laser melting of metals enabled by new high-fidelity multiphase, multiphysics computational tool', *Computer Methods in Applied Mechanics and Engineering* 399 (2022), 115422, https://doi.org/10.1016/j.cma.2022.115422.

[19] M. SCHRETER-FLEISCHHACKER, N. MUCH, P. MUNCH, M. KRONBICHLER, W. A. WALL, C. MEIER: 'A consistent diffuse-interface finite element approach to rapid melt–vapor dynamics with application to metal additive manufacturing', *Computer Methods in Applied Mechanics and Engineering* 442 (2025), 117985, https://doi.org/10.1016/j.cma.2025.117985.

[20] M. COURTOIS, M. CARIN, P. L. MASSON, S. GAIED, M. BALABANE: 'A new approach to compute multi-reflections of laser beam in a keyhole for heat transfer and fluid flow modelling in laser welding', *J. Phys. D: Appl. Phys.* 46 (2013), 505305, https://doi.org/10.1088/0022-3727/46/50/505305.

[21] T. F. FLINT, L. SCOTTI, H. C. BASOALTO, M. C. SMITH: 'A thermal fluid dynamics framework applied to multi-component substrates experiencing fusion and vaporisation state transitions', *Commun. Phys.* 3 (2020), 196, https://doi.org/10.1038/s42005-020-00462-7.

[22] T. F. FLINT, J. D. ROBSON, G. PARIVENDHAN, P. CARDIFF: 'laserbeamFoam: Laser ray-tracing and thermally induced state transition simulation toolkit', *SoftwareX* 21 (2023), 101299, https://doi.org/10.1016/j.softx.2022.101299.

[23] W. TAN, Y. C. SHIN: 'Analysis of multi-phase interaction and its effects on keyhole dynamics with a multi-physics numerical model', *J. Phys. D: Appl. Phys.* 47 (2014), 345501, https://doi.org/10.1088/0022-3727/47/34/345501.

[24] C. ZENZ, M. BUTTAZZONI, T. FLORIAN, K.E. CRESPO ARMIJOS, R. GÓMEZ VÁZQUEZ, G. LIEDL, A. OTTO: 'A compressible multiphase Mass-of-Fluid model for the simulation of laser-based manufacturing processes', *Computers & Fluids* 268 (2024), 106109, https://doi.org/10.1016/j.compfluid.2023.106109.

[25] F. YANG, X. MENG, S.N. PUTRA, A. ARTINOV, M. BACHMANN, M. RETHMEIER: 'Numerical analysis of the effect of an oscillating metal vapor plume on the keyhole and molten pool behavior during deep penetration laser beam welding', *J. Laser Appl.* 35 (2023), 042041, https://doi.org/10.2351/7.0001094.

[26] D. COVIELLO, A. D'ANGOLA, D. SORGENTE: 'Numerical Study on the Influence of the Plasma Properties on the Keyhole Geometry in Laser Beam Welding', *Front. Phys.* 9 (2022), https://doi.org/10.3389/fphy.2021.754672.

[27] N. SCHELL, A. KING, F. BECKMANN, T. FISCHER, M. MÜLLER, A. SCHREYER: 'The High Energy Materials Science Beamline (HEMS) at PETRA III', *Materials Science Forum* 772 (2014), 57-61, https://doi.org/10.4028/www.scientific.net/MSF.772.57.

[28] T. STAUDT, E. ESCHNER, F. TENNER, M. SCHMIDT: 'Deriving spectral information upon the laser welding process employing a hyperspectral imaging technique', *Procedia CIRP* 74 (2018), 636-639, https://doi.org/10.1016/j.procir.2018.08.061.

[29] A. ZAKIROV, S. BELOUSOV, M. BOGDANOVA, B. KORNEEV, I. ISKANDAROVA, A. PEREPELKINA, B. POTAPKIN, 'KiSSAM: efficient simulation of melt pool dynamics during PBF using GPUs', *Prog. Addit. Manuf.* 9 (2024), 1491-1508, https://doi.org/10.1007/s40964-023-00561-1.

[30] D.S. NAKAPKIN, A.V. ZAKIROV, S.A. BELOUSOV, M.V. BOGDANOVA, B.A. KORNEEV, A.E. STEPANOV, A.Y. PEREPELKINA, V.D. LEVCHENKO, A. MESHKOV, 'Finding optimal parameter ranges for laser powder bed fusion with predictive modeling at mesoscale', *2nd International Conference on Simulation for Additive Manufacturing* (2019), 297-308.

[31] B. KORNEEV, A. ZAKIROV, M. BOGDANOVA, S. BELOUSOV, A. PEREPELKINA, I. ISKANDAROVA, B. POTAPKIN, 'A numerical study of powder wetting influence on the morphology of laser powder bed fusion manufactured thin walls', *Additive Manufacturing* 74 (2023), 103705, https://doi.org/10.1016/j.addma.2023.103705.

[32] M. BOGDANOVA, S. CHERNYSHIKHIN, A. ZAKIROV, B. ZOTOV, L. FEDORENKO, S. BELOUSOV, A. PEREPELKINA, B. KORNEEV, M. LYANGE, I. PELEVIN, I. ISKANDAROVA, E. DZIDZIGURI, B. POTAPKIN, A. GROMOV, 'Mesoscale Simulation of Laser Powder Bed Fusion with an Increased Layer Thickness for AlSi10Mg Alloy', *Journal of Manufacturing and Materials Processing* 8 (2024) 7, https://doi.org/10.3390/jmmp8010007.

[33] A. ZAKIROV, S. BELOUSOV, M. BOGDANOVA, B. KORNEEV, A. STEPANOV, A. PEREPELKINA, V. LEVCHENKO, A. MESHKOV, B. POTAPKIN: 'Predictive modeling of laser and electron beam powder bed fusion additive manufacturing of metals at the mesoscale', *Additive Manufacturing* 35 (2020), 101236, https://doi.org/10.1016/j.addma.2020.101236.

[34] T. KRÜGER, H. KUSUMAATMAJA, A. KUZMIN, O. SHARDT, G. SILVA, E.M. VIGGEN: 'The Lattice Boltzmann Method: Principles and Practice', *Springer International Publishing*, Cham, 2017, https://doi.org/10.1007/978-3-319-44649-3.

[35] M. BAUER, S. EIBL, C. GODENSCHWAGER, N. KOHL, M. KURON, C. RETTINGER, F. SCHORNBAUM, C. SCHWARZMEIER, D. THÖNNES, H. KÖSTLER, U. RÜDE: 'waLBerla: A block-structured high-performance framework for multiphysics simulations', *Computers & Mathematics with Applications* 81 (2021) 478-501, https://doi.org/10.1016/j.camwa.2020.01.007.

[36] CHAIR FOR SYSTEM SIMULATION, 'waLBerla (widely applicable Lattice Boltzmann from Erlangen)', (2025), https://doi.org/10.5281/zenodo.16760078.

[37] D. R. NOBLE, J. R. TORCZYNSKI: 'A Lattice-Boltzmann Method for Partially Saturated Computational Cells', *Int. J. Mod. Phys. C* 09 (1998), 1189-1201, https://doi.org/10.1142/S0129183198001084.

[38] R. ZHANG, H. FAN, H. CHEN: 'A lattice Boltzmann approach for solving scalar transport equations', *Phil. Trans. R. Soc. A.* 369 (2011), 2264-2273, https://doi.org/10.1098/rsta.2011.0019.

[39] M. MARKL, A. M. RAUSCH, V. E. KÜNG, C. KÖRNER: 'SAMPLE: A Software Suite to Predict Consolidation and Microstructure for Powder Bed Fusion Additive Manufacturing', *Advanced Engineering Materials* 22 (2020), 1901270, https://doi.org/10.1002/adem.201901270.

[40] M. BAUER, J. HÖTZER, D. ERNST, J. HAMMER, M. SEIZ, H. HIERL, J. HÖNIG, H. KÖSTLER, G. WELLEIN, B. NESTLER, U. RÜDE: 'Code generation for massively parallel phase-field simulations', in: *Proceedings of the International Conference for High Performance Computing*, Networking, Storage and Analysis, ACM, Denver Colorado, 2019, pp. 1-32. https://doi.org/10.1145/3295500.3356186.

[41] CHAIR FOR SYSTEM SIMULATION (Friedrich-Aalexander-Universität Erlangen-Nürnberg), 'pystencils', (2024), https://doi.org/10.5281/zenodo.15276904.

[42] M. BAUER, H. KÖSTLER, U. RÜDE: 'lbmpy: Automatic code generation for efficient parallel lattice Boltzmann methods', *Journal of Computational Science* 49 (2021), 101269, https://doi.org/10.1016/j.jocs.2020.101269.

[43] F. HENNIG, M. HOLZER, U. RÜDE: 'Advanced Automatic Code Generation for Multiple Relaxation-Time Lattice Boltzmann Methods', *SIAM J. Sci. Comput.* 45 (2023), C233-C254, https://doi.org/10.1137/22M1531348.

[44] CHAIR FOR SYSTEM SIMULATION (Friedrich-Alexander-Universität Erlangen-Nürnberg), 'lbmpy', (2024), https://doi.org/10.5281/zenodo.15277053.

[45] J. GÖTZ, K. IGLBERGER, C. FEICHTINGER, S. DONATH, U. RÜDE: 'Coupling multibody dynamics and computational fluid dynamics on 8192 processor cores', *Parallel Computing* 36 (2010), 142-151, https://doi.org/10.1016/j.parco.2010.01.005.

[46] A. KLASSEN, T. SCHAROWSKY, C. KÖRNER: 'Evaporation model for beam based additive manufacturing using free surface lattice Boltzmann methods', *J. Phys. D: Appl. Phys.* 47 (2014), 275303. https://doi.org/10.1088/0022-3727/47/27/275303.

[47] J. TRAPP, A.M. RUBENCHIK, G. GUSS, M.J. MATTHEWS: 'In situ absorptivity measurements of metallic powders during laser powder-bed fusion additive manufacturing', *Applied Materials Today* 9 (2017), 341-349, https://doi.org/10.1016/j.apmt.2017.08.006.

[48] M. HOLZER, M. BAUER, H. KÖSTLER, U. RÜDE: 'Highly efficient lattice Boltzmann multiphase simulations of immiscible fluids at high-density ratios on CPUs and GPUs through code generation', *The International Journal of High Performance Computing Applications* 35 (2021), 413-427, https://doi.org/10.1177/10943420211016525.

[49] M. HOLZER, G. STAFFELBACH, I. ROCCHI, J. BADWAIK, A. HERTEN, R. VAVRIK, O. VYSOCKY, L. RIHA, R. CUIDARD, U. RÜDE: 'Scalable Flow Simulations with the Lattice Boltzmann Method', in: *Proceedings of the 20th ACM International Conference on Computing Frontiers*, Association for Computing Machinery, New York, NY, USA, 2023, pp. 297-303, https://doi.org/10.1145/3587135.3592176.

[50] H. SCHOTTENHAMML, A. ANCIAUX SEDRAKIAN, F. BLONDEL, H. KÖSTLER, U. RÜDE: 'waLBerla-wind: A lattice-Boltzmann-based high-performance flow solver for wind energy applications', *Concurrency and Computation: Practice and Experience* 36 (2024), e8117, https://doi.org/10.1002/cpe.8117.

[51] M. HOLZER: 'Code generation in a lattice Boltzmann framework for exascale computing', 2025, https://open.fau.de/handle/openfau/33506 (accessed January 15, 2025).

[52] M. GEIER, M. SCHÖNHERR, A. PASQUALI, M. KRAFCZYK: 'The cumulant lattice Boltzmann equation in three dimensions: Theory and validation', *Computers & Mathematics with Applications* 70 (2015), 507-547, https://doi.org/10.1016/j.camwa.2015.05.001.

[53] S. KEMMLER, C. RETTINGER, U. RÜDE, P. CUÉLLAR, H. KÖSTLER: 'Efficiency and scalability of fully-resolved fluid-particle simulations on heterogeneous CPU-GPU architectures', (2024), https://doi.org/10.48550/arXiv.2303.11811.